

Partial self-ordering observed in silicon nanoclusters deposited on silicon oxide substrates by chemical vapor deposition

R. A. Puglisi,* G. Nicotra, S. Lombardo, and C. Spinella

Istituto per la Microelettronica e Microsistemi, Consiglio Nazionale delle Ricerche, Sezione di Catania, Stradale Primosole 50 95121 Catania, Italy

G. Ammendola and C. Gerardi

STMicronics, Stradale Primosole 50 95121 Catania, Italy

(Received 8 April 2004; revised manuscript received 13 September 2004; published 21 March 2005)

The formation of Si dots by chemical vapor deposition is studied from the very early stages of the dot formation up to about 25% of substrate coverage. Structural characterization is mainly performed by means of energy filtered transmission electron microscopy, which couples chemical information to very high spatial resolution. The dots are shown to be surrounded by Si-free regions and this is attributed to the Si adatom capture mechanism from each nucleus. The data are discussed in the framework of a self-similar model, which takes into account the dot local environment, the adatom diffusion and the continuous nucleation of new islands. From the fit to the data the correlation between the dot size and the capture area is obtained and the number of deactivated nucleation sites is quantified.

DOI: 10.1103/PhysRevB.71.125322

PACS number(s): 81.07.Ta, 81.15.Gh, 68.37.Lp, 89.75.Da

I. INTRODUCTION

The storage of electrical charge in silicon nanodots has stimulated considerable effort to understand its mechanism and utilize it to fabricate nonvolatile memory (NVM) devices.¹⁻⁶ The main advantage of using discrete charge storage nodes, respect to the conventional continuous floating gates, is the high reliability associated with the localized traps. In discrete trap memories, in fact, a single leakage path due to a defect (intrinsic or stress induced) in the oxide can only discharge a single storage node. Among the other methods of synthesis, like ion implantation or aerosol, a well established way to obtain Si quantum dots for application in NVM is the chemical vapor deposition (CVD), because it is fully compatible with standard integrated circuit technology and the deposition parameters are well controlled. Moreover the stoichiometric SiO₂ matrix allows one to obtain electrically isolated storage nodes. Many results exist in literature on the tunability of the CVD process, through the deposition parameters,^{1,7,24} or substrate pretreatments,^{8,9} in order to obtain high Si nanodot density and controlled size, which are important requirements for the device application. Together with the dot density and size, the distance between the dots is also a fundamental parameter, because it has a direct impact on the robustness of the device, with respect to the defects in the tunnel oxide.¹⁰ The charge transfer mechanism between the dots, in fact, actually contributes to the charge dispersion, all over the gate, and to the consequent loss of the stored information. So it is important to fully understand the mechanisms which govern both the final dot size and the spatial distribution. Previously we have reported a systematic experimental observation on the size distribution¹¹ and the interdot distance¹² at several deposition temperatures, times and chemical substrate pretreatment of Si dots obtained by CVD on SiO₂. The results indicate that new Si dots continuously form on the substrate, also after long deposition times,

hence at high substrate coverage. The silicon dots are found to preferentially nucleate at distances longer than at least 4 nm from the edge of existing dots. Similar results are also found by covering the dots with a cap layer of CVD SiO₂, by changing the deposition temperature, the oxide thickness and the chemical conditions of the substrate before the deposition.¹³ These results evidence the existence of a capture zone centered around each dot, within which the silicon adatoms are preferentially captured by the pre-existing dot rather than aggregate to form a new nucleus. The silicon adatom, in fact, after the dissociation from the SiH₄ molecule on a physisorption site of the surface, can contribute either to the formation of a new island, but also to the growth of a pre-existing dot via surface diffusion. These local fluctuations in the environment of the silicon islands are neglected in the classical mean field nucleation theory, but play a role in the final size and spatial distribution of the dots. In the preceding work cited above we have shown that this theory can fit very well the dot size distribution, but fails in the fit of the nearest-neighbor edge distance distribution. Many theoretical approaches exist in literature on the adatom capture mechanism, and the simulation results have been well compared to experimental data relative to Ga clusters on GaAs substrates,¹⁴ and Sn,¹⁵ Ge (Ref. 16) or AlQ₃ on Si substrates.¹⁷ All these data, however, refer to materials obtained through high vacuum evaporation methods. The modeling of the silicon nanoclusters formation by CVD however has not found much popularity in literature, with respect, for example, to the synthesis through ion implantation, because of the many parameters ruling the nucleation of the Si islands (adatoms diffusion, evaporation, local deactivation of nucleation sites), which exclude the possibility to use the classical mean field nucleation theories. Moreover the weak contrast difference between the silicon and the silicon dioxide, during TEM imaging, gives rise to the experimental difficulty of characterizing silicon nanostructures formed on, or

embedded in, silicon oxide, with proper high resolution and large statistics. Many interesting experiments have been proposed in literature in order to characterize these structures, like, for example, decorating the surface of the silicon nanodots through ion implantation of foreign materials.¹⁸ The present work is a structural characterization of silicon nanoclusters formed by chemical vapor deposition. The characterization is performed at very high spatial resolution (0.5 nm), by using energy filtered transmission electron microscopy (EFTEM), which couples standard TEM analysis to the compositional information obtained by in situ electron energy loss spectroscopy. The main aspects related to the characterization of the Si dots through EFTEM, like the imaging conditions, the identification of the Si respect to the SiO₂ and a comparison with the results obtained from other experimental techniques, are already reported elsewhere,^{19,20} and are summarized in the next paragraph. The experimental measurements obtained by EFTEM on the dot size and nearest-neighbor edge distances are reported in the “Results and Discussion” section. The calculations of the capture zone patterns, obtained through a method which takes into account also the dot size dispersion due to the continuous nucleation, are also presented. The dependence of the final dot size on the available capture size is presented for several substrate coverage. The experimental data, new in literature at our best knowledge, are discussed with respect to a model based on the modification of the Voronoi tessellation. The fit to the data provides the number of nucleation sites deactivated by the silicon adatom capture mechanism.

II. EXPERIMENT

The reactor used for the nanodot synthesis is a rapid thermal CVD (RTCVD) system with air cooled tungsten lamps that allow temperature transitions on the surface of the wafers as fast as 50 °C/s, while maintaining the walls of the deposition chamber at much lower temperatures. The Si dots were deposited on 8 in. oxidized *p*-type Si substrates with wet oxides of 10 nm of thickness. The depositions are operated at temperatures between 500 °C and 550 °C, at chamber pressure of 80 Torr, with SiH₄ as Si precursor and with H₂ as carrier gas, with a total gas flux of 9.3 l/s, and with a SiH₄ flux of 0.4 l/s. In order to characterize the Si nanodots several characterization techniques have been exploited like scanning electron microscopy (SEM) equipped with field emission gun, atomic force microscopy (AFM) with sharp tips, high resolution TEM (HRTEM), dark field (DF), and energy filtered TEM (EFTEM). A special attention has been devoted to this point because of the difficulty to identify the silicon phase of the dots respect to the oxide phase of the substrate. The results of the investigation have been already reported elsewhere.¹⁹ The main result of this study is that if another chemical element is covering the Si dots AFM or SEM show some limits, because it is not possible to distinguish between the silicon phase and the shell of foreign material, so the dots appear with larger size than the real one. In studying Si nanodots on SiO₂ also the HRTEM and DF show limits, since these methods generally require to have the Si dots in the crystalline phase, rather than in the amorphous

one. Moreover, even if the dots are crystalline, in order to observe the lattice planes, the dots must be in Bragg conditions, i.e., properly oriented respect to the electron beam. This greatly restricts the number of dots visible during the analysis. To study the morphology of samples with very high numbers of small Si dots, crystalline or amorphous, and deposited on oxidized Si substrates, we have found that a suitable technique is the energy filtered TEM (EFTEM). It couples a very high spatial resolution (0.5 nm) to a compositional information obtained by in situ electron energy loss spectroscopy. This analysis has been carried out by using a JEOL JEM 2010F TEM operating at 200 kV accelerating voltage and equipped with a field emission gun. The energy filtering system is a Gatan GIF based on a magnetic-prism spectrometer and a 2k × 2k multiscan CCD camera. The energy-selecting window used to image the Si nanocrystals is 4 eV centered at 16 eV energy loss, i.e., close to the Si bulk plasmon value. The contrast in this case is independent of the phase of the dots, i.e., whether crystalline or amorphous. The contrast difference between Si and SiO₂ is due to the difference in plasmon energy loss of the two materials and this will be detailed in the next section. The EFTEM plan view micrograph obtained at 16 eV is elaborated by suitable computer image processing and it is transformed in a black and white image. The transformed images can then be analyzed and the corresponding Si dot area and positions can be estimated. The radius of each dot is taken as $r_d = \sqrt{A_d/\pi}$, where A_d is the area of the dot. From the dot radius and the position of its centroid, we also measure the nearest neighbor distance d between the edges of the dots. The distributions have been obtained by considering a statistics of about 500 dots per sample.

A. Si dots oxidation

By means of EFTEM it is possible to identify the presence of a shell of oxide over the dots and to measure its thickness. This is possible by taking images at 16 eV, close to the silicon bulk plasmon loss value and at 26 eV, close to the SiO₂ plasmon loss value. Figure 1(a) shows a EFTEM micrograph in plan view of a Si nanodot sample subjected to an oxidation process. The image is obtained by selecting 16 eV of energy loss. The white spots correspond to the silicon region on the sample. The same portion of the sample is then observed at 26 eV, and the corresponding image is reported in Fig. 1(b). Now the white parts correspond to the SiO₂ regions, thicker respect to the substrate. In particular, the white circles indicate two dots which have been partially oxidized during the oxidation process. They appear with larger size at 26 eV due to the presence of the SiO₂ shell. By comparing the two analysis it is possible to measure the oxide shell thickness for each dot. For example, for the two dots in the circle it has been found to be about 2 nm. At 26 eV it is also possible to evidence the presence of Si dots which have been completely oxidized. The arrows in Fig. 1(b) indicate few examples of this situation. As it is possible to observe the remaining SiO₂ phase is well visible at 26 eV, although the silicon phase has completely disappeared in the corresponding regions [arrows in Fig. 1(b)]. This analysis

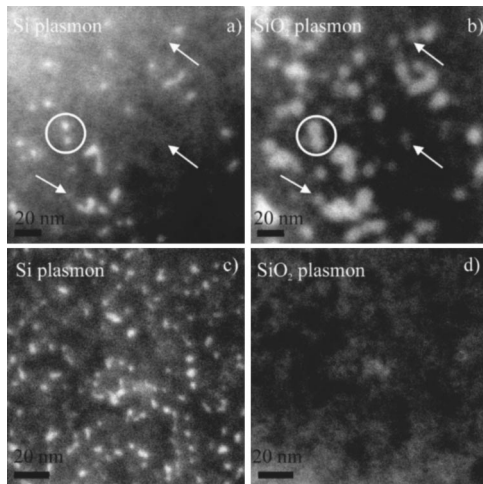


FIG. 1. EFTEM micrographs of a Si sample subjected to strong oxidation, taken (a) on the Si, and (b) on the SiO₂ plasmon loss. The circles indicate two dots not completely oxidized. The arrows in (b) indicate completely oxidized Si dots. Indeed, in the corresponding regions the Si phase is not visible at 16 eV [arrows in (a)]. (c) and (d) EFTEM micrographs of a typical as deposited Si nanodot sample taken at 16 eV, and at 26 eV, respectively.

shows that completely oxidised Si dots, when present, are clearly evidenced by EFTEM.

The experiments reported in the paper regard samples as deposited and not subjected to any oxidation process. The samples however have been exposed to the air, in the lack of time (of the order of days) between the deposition and the analysis by EFTEM. In order to observe the oxidation of the Si dot samples in air, we have systematically performed analysis at 16 eV and at 26 eV on all the samples. Figure 1 reports a typical example of this analysis, obtained at 16 eV (c) and at 26 eV (d). As it is possible to see the analysis at 26 eV shows a uniform background due to the SiO₂ substrate, thus indicating that there are no local variations in the oxide thickness. This indicates that negligible oxidation has been observed on these samples after deposition. The fact that no oxidation is evident after air exposure seems in contrast with the well-known rapid oxidation rate of the Si in air, responsible for the immediate formation of the 1.5 nm thick native oxide. The contrast is probably only apparent. We should consider in fact that the size of the Si dots here investigated is ranging between about 1 and 4 nm in radius, i.e., structures very different from a planar surface. Small dots of about this size, and subjected to oxidation processes, have already been studied by other groups^{21–23} and a strong retardation, respect to the planar Si, has been experimentally observed also in these cases. This literature generally agrees on the fact that, based on the experimental evidence, the Deal-Grove model does not apply to the oxidation of Si nanodots. The responsibility for this behavior has been indicated by these groups in the compressive stress appearing inside the dot due to the volume difference of SiO₂ and Si. This compressive stress reduces the reaction rate for the Si nanodots surface oxidation.

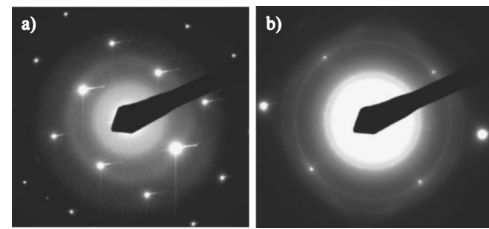


FIG. 2. Diffraction patterns relative to samples of Si dots after deposition at 550 °C for 90 s (a), and after annealing at 1000 °C for 40 s (b).

B. Thermodynamical phase of the Si dots

Another important aspect is the study on the thermodynamical phase of the deposited dots. It has been found by diffraction analysis that the silicon dots are in the amorphous phase up to 550 °C of deposition temperature. Figure 2 shows the diffraction patterns relative to samples of Si dots after deposition at 550 °C for 90 s (a), and after annealing at 1000 °C for 40 s (b). The analysis has been performed in a region where the Si substrate was not removed, and this allows to show that the Si dots ring and the diffraction spots due to the crystalline Si are at the same distance respect to the transmitted beam. As can be seen in Fig. 2(a), the diffraction pattern shows a wide ring indicating that no crystalline phases are present in the as deposited material, although the sample has been deposited at the highest temperature here investigated. After annealing the sample is crystallized, as demonstrated by the image in (b), where the diffraction ring, demonstrates the presence of small crystalline structures. The same result has been observed in Si dot samples which have been immediately covered by a 7 nm thick CVD oxide after deposition, thus suggesting that the amorphous state is not the result of other ex-situ transformations. Other results in literature report that by using low pressure chemical vapor deposition (LPCVD) operating at pressures of about 200–300 mTorr,^{7,24} the as deposited silicon dots are crystalline. This is in contrast with the results that we have obtained in our samples. It should be however considered that the samples here described are fabricated in a RTCVD operating at very high pressures (80 Torr) and low temperatures (500 °C–550 °C), with all the deposition parameters tuned to guarantee very high speed of deposition (0.05 nm/s at 550 °C for 400 sccm of silane flux). The large difference in the chamber pressure and in the deposition rate are probably responsible for the fact that the silicon dots do not nucleate in the crystalline phase.

III. RESULTS AND DISCUSSION

Figures 3(a)–3(c) report the EFTEM micrographs in plan view of the samples deposited at 500 °C for increasing times, 600 s, 750 s, and 900 s, respectively. The white spots represent the silicon nanodots on the silicon oxide substrate, which is the dark background. As it is possible to observe from Fig. 3 the number and the size of the Si dots increase with the deposition time. Specifically the dot density increases from $3 \times 10^{11} \text{ cm}^{-2}$ up to $7 \times 10^{11} \text{ cm}^{-2}$, reached af-

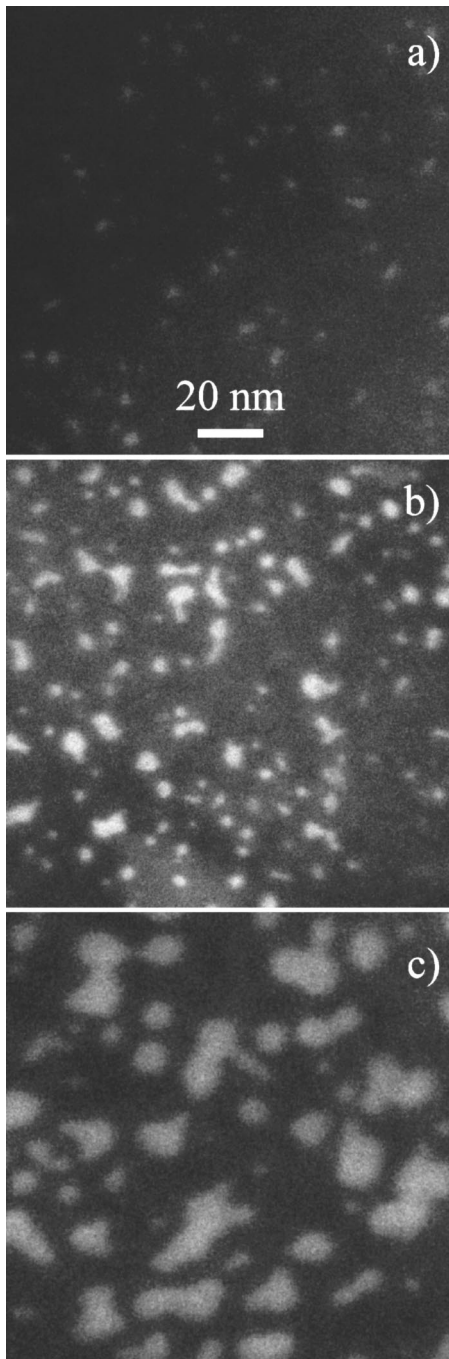


FIG. 3. Sequence of EFTEM micrographs in plan view of Si quantum dot layers, deposited at 500 °C for 600 s, with coverage 1.8% (a), 750 s for 14.7% (b), and 900 s for 28% (c).

ter 750 s of deposition, and then, because of the impingement between the dots, it decreases to about $3 \times 10^{11} \text{ cm}^{-2}$. The appearance of new Si dots during the deposition is a strong indication that the nucleation process is continuous. The covered fraction increases from 2% to almost 30%. Figure 4 reports the dot radius, r_d [Fig. 4(a)], and the nearest neighbor edge distance, d [Fig. 4(b)], frequency distributions for the samples deposited at 525 °C for 200 s (squares), with coverage of 14.1%, and at 550 °C for 90 s (circles) which exhibits a coverage of 14%. The radius frequency distribu-

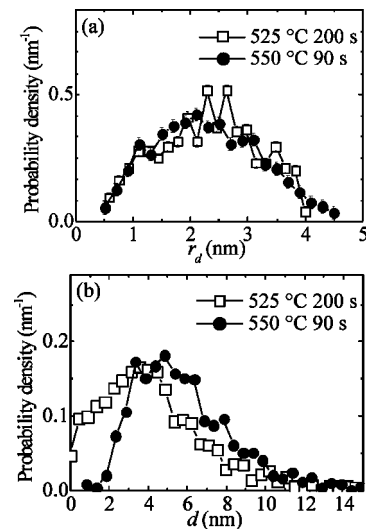


FIG. 4. Dot radius r_d (a) and nearest neighbor edge distance d (b) distributions for samples deposited at 525 °C for 200 s (squares), and 550 °C for 90 s (circles). Both samples show similar substrate coverage of about 14%.

tions $f(r_d)$ have been obtained by a statistical analysis of 500 dots, and subsequent binning (20 bins) over the same radius interval. The median values of $f(r_d)$ are 2.2 nm in both cases. Despite of the different deposition parameters, the two distributions relative to samples with similar coverage are very similar. The dot size distributions are well fitted for all the different coverage cases, by adopting a model of continuous nucleation in the approximation of capillarity, modified to take into account the dot coalescence contribution.²⁵ Through the fit to the experimental data, an activation energy for the nucleation process of about 0.3 eV is found.¹¹ While the dot size distribution is easily comparable for the two samples, the spatial distribution of the dots presents a more complicated behavior. Indeed, as it is possible to observe from Fig. 4(b), the number of dots which nucleates closer than about 3–4 nm to other pre-existing dots, is very low. A similar result is obtained by changing the oxide thickness, by covering the dots with a 7 nm cap layer of oxide, and by changing the surface chemical treatment before the deposition.^{12,13} A possible explanation to the shape of the $f(d)$ can be related to a mechanism of Ostwald Ripening (OR) during the deposition. In order to quantify the possible contribution to the depleted zone coming from OR during the deposition, we have annealed the samples at the same temperatures and times used for the deposition processes. After annealing, the EFTEM analysis does not show any appreciable change in the edge distance distribution of the dots, for annealing temperatures up to 550 °C and for times shorter than 900 s, respectively, corresponding to the highest deposition temperature and longest deposition time here investigated. So it is possible to exclude the OR as responsible for the peaked shape of the curves in Fig. 4(b). These results can instead be explained in terms of silicon adatom diffusion and capture mechanisms. In particular the silicon adatoms, obtained from the dissociation of the silane, before aggregating to form a new nucleus, can diffuse toward previously

nucleated clusters. So it is possible to define a capture zone centered around every nucleus where all the silicon adatoms, which fall within it, will preferentially contribute to the growth of this nucleus (for a complete review see, for example, Ref. 26). In this condition the new nucleation event in the depletion region around each dot is strongly reduced and the nucleation site deactivated. As they spread with time, the capture zones may overlap adjacent active nucleation sites on which nuclei have not yet formed.²⁷ One of the theoretical approaches present in literature simulates such a capture zone by using the Voronoi tessellation,²⁸ for each dot it can be defined a boundary enclosing all the intermediate points lying closer to the center of this dot than to other points on the substrate. In this way the growth rate of each dot is limited by the diffusion of the deposited monomers, and depends on how much free substrate it has in its immediate neighborhood. Figure 5(b) reports an example of the Voronoi tessellation relative to a sample deposited at 550 °C for 90 s. The pattern has been obtained by considering the dot centroid and radius obtained from the analysis of the EFTEM image in plan view of the sample [Fig. 5(a)]. The dotted circles in the Fig. 5(b) have been superposed on to the Voronoi lattice, after the calculation of the pattern, and represent the Si dots, approximated to circles, with their centroid. As it is also possible to observe in Fig. 5(b), small nuclei have Voronoi polygons of sizes similar to the ones of large nuclei. So large dots could tend to outgrow their Voronoi polygons, spilling over into the polygons of smaller neighbors. For this reason the Voronoi tessellation provides a good interpretation of the experiment only in the heterogeneous nucleation case, where the nuclei form almost at the same time in the very early stages of the deposition, and the dot growth proceeds by only including adatoms falling in each own capture zone. In this case the dot size distribution appears very sharp. In our case, the formation of new nuclei during the deposition, i.e., the increment in the dot density with the deposition time, as discussed for Figs. 3(a) and 3(b) is a clear indication that the nucleation process is continuous. As a consequence, the Voronoi approach cannot provide a realistic interpretation of the dot growth process. In the case of homogeneous nucleation, in fact, it should be also considered that late nuclei do continue to form, and they are surrounded by dots of significant extent, which reduce the area of their capture zone. So in the case of homogeneous nucleation it has been proposed that the boundary of the true capture zone lies at the center of the edge distance between the dots.²⁹ In order to properly quantify the monomer diffusion contribution, the capture zone pattern has been calculated for all the investigated cases. Figure 5(c) reports the one relative to the sample imaged in Fig. 5(a). Also in the case of Fig. 5(c) the circles representing the dots have been superposed, as a guide for the eye, in order to easily compare the dot size to its capture size.

As it is possible to note from the comparison with Fig. 5(b), late nuclei have capture zones smaller than their Voronoi polygons, as expected. Moreover the boundaries of the capture zones are slightly curved rather than straight lines, because they follow the dot boundary. The dots at the boundaries of the figures, because of the contribution of the dots falling out of the observed region, presumably have cap-

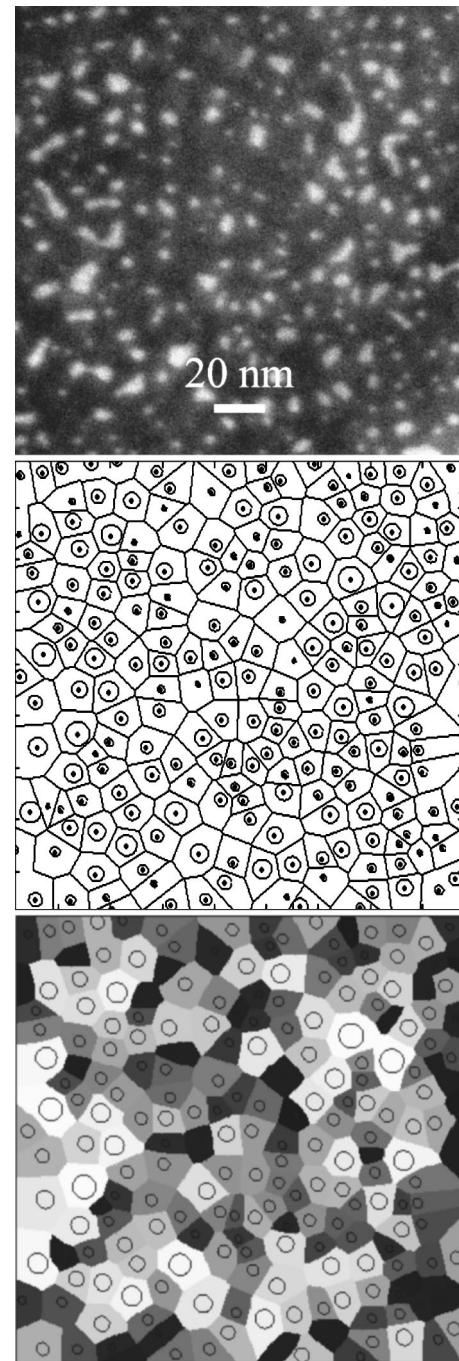


FIG. 5. (a) EFTEM micrograph in plan view of a Si quantum dot layer, formed at 550 °C for 90 s, (b) computed Voronoi tessellation, and (c) capture zone pattern.

ture areas smaller than the ones obtained by the calculation, so they have not been taken into account in all the following calculations. By using the capture zone size calculated with this method we obtain very good correlation with the radius size, as displayed by the graphs reported in Fig. 6 as examples. They show the scaled dot radius $r_d/\langle r_d \rangle$ as a function of the corresponding scaled capture radius, $r_c/\langle r_c \rangle$, for the samples deposited at 550 °C for 90 s [Fig. 6(a)], and 550 °C for 100 s [Fig. 6(b)]. The samples, respectively, show a coverage θ of 14% and 14.5%. As it is possible to observe, the

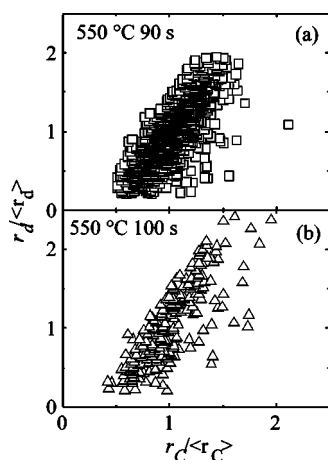


FIG. 6. Correlation between the scaled radius of the Si dot $r_d/\langle r_d \rangle$ and the scaled capture radius $r_c/\langle r_c \rangle$, for the samples deposited at 550 °C for 90 s with 14% (a) and 550 °C for 100 s with 14.5% (b).

scaled dot radius increases with the scaled capture radius, and the data lie close to the graph bisectrix. The data points do not pass for the graph origin. This can be addressed to the finite size of the smallest dot observed in our measurements ($r_d \leq 0.5$ nm), and its relative capture area. It has however been found that by removing from the calculations all the dots with radius $r_d = 0.9$ nm, which corresponds to intentionally increase the minimum observed dot radius, the results of Fig. 6, and also the following calculations, do not show important differences. The results of Fig. 6, relative to samples with coverage going from 14% to 14.5%, suggest that the dependence of the scaled dot radius $r_d/\langle r_d \rangle = r'_d$ on the scaled capture radius $r_c/\langle r_c \rangle = r'_c$ increases as a function of the coverage. In fact, we have computed the capture zone pattern for all the samples and followed the dependence of r'_d on r'_c , i.e.,

$$r'_d = k(r'_c)^\sigma, \quad (1)$$

for several coverage and before the strong coalescence takes place. By using the following equation, $\log_{10}(r'_d) = \log_{10}(k) + \sigma \log_{10}(r'_c)$, the dependence of σ on the substrate coverage θ has been obtained, and the results are reported in Fig. 7. The dotted and solid lines plotted in the graph represent the values of σ when the scaled dot volume [$\propto (r'_d)^3$] or the scaled dot area [$\propto (r'_d)^2$], respectively, depend on the capture area. As it is possible to see from the data of Fig. 7, σ increases as a function of the coverage θ and tends to saturate at about $\theta = 25\%$. For $\theta < 5\%$ σ exhibits very low values, and this suggests no correlation between the dot radius and the capture zone. For coverage $\theta \geq 5\%$ however σ shows increasing values and this suggests that the effect of the capture zone increases. At $\theta \approx 6\%$ we obtain $\sigma = 0.66$, which indicates that the normalized dot volume depends on the normalized capture area [three dimensional (3D)]. The normalized dot area depends on the normalized capture area [two dimensional (2D)] for $\theta \approx 8\%$. Despite of the different synthesis conditions, samples which have similar coverage exhibit also similar values of σ . This is demonstrated by the

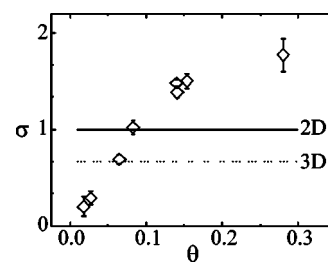


FIG. 7. Correlation between σ defined as $\log_{10}(r'_d) = \log_{10}(k) + \sigma \log_{10}(r'_c)$ as a function of coverage θ . The values of θ for a two- and three-dimensional dependence of r'_d from $(r'_c)^2$, i.e., from the scaled capture area, are indicated by the solid and dotted lines, respectively.

points at $\theta \approx 14\%$, which correspond to samples deposited at 525 °C (200 s), 550 °C (90 s), and 500 °C (750 s), respectively. This indicates that the parameter which governs the self-similar properties of the dot growth process is the coverage θ . The linear correlation coefficient obtained from the fit to the data has been measured and it increases as a function of the coverage θ , ranging between 0.8 and 1 for $\theta \geq 8\%$, i.e., in the range where the capture zone governs the dot growth process. From the fit to the experimental data we have also found a value of k [see Eq. (1)] similar for all the samples, and this value is about 0.9, which gives rise to the following expression for the scaling behavior observed in this experiment $r'_d = 0.9(r'_c)^\sigma$.

In order to fit the data relative to the dot radius distribution $f(r_d)$, it has also been shown, for nonrandom nucleation simulated processes, that if we rescale each distribution using the time-dependent length scale factor, $r_d/\langle r_d \rangle = r'_d$, the $f(r'_d)$ can be fitted by the following expression:

$$F(y) = \frac{\beta_r^{\beta_r}}{\Gamma(\beta_r)} y^{\beta_r-1} \exp(-\beta_r y), \quad (2)$$

where y is the scaled dot radius r'_d and β_r is a free parameter.²⁹ Figure 8 reports, as an example, the scaled radius distributions for the samples deposited at 500 °C for 750 s (a) and at 550 °C for 80 s (b). The solid lines represent the fit results obtained by Eq. (2) with $\beta_r = 8$. As it is possible to observe, the curves fit the experimental data with very good agreement. This confirms that the Si dots formation process is not fully random and that the system evolves by self-ordering, albeit only partially. By numerical simulations, it has been found that $\beta_r = 8$ corresponds to a Voronoi network where 30% of initially random points are excluded from the system and then deactivated like possible nucleation sites by the nearest neighbor exclusion mechanism. As a confirmation of the correctness of the fit procedure applied in Fig. 8, the values for β_r obtained from the fit, have been compared to the polydispersity ratio, defined as $\langle r_d \rangle^2 / \text{std}_r^2$, between the mean value $\langle r_d \rangle$ and the variance std_r^2 of $f(r_d)$, and the results are reported in Table I. The comparison shows that the values obtained from the two procedures are in very good agreement. This confirms that the analytical form of the $f(r_d)$ is well described by a Γ function. The observed deviation at high coverage (15% and 28%) is at-

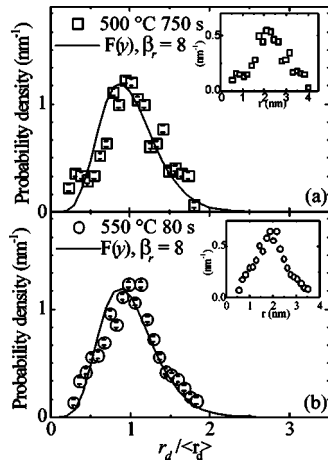


FIG. 8. Distributions of the normalized dot radius, $r_d/\langle r_d \rangle$, for the samples deposited at 500 °C for 750 s, with coverage of 14.7% (a) and at 550 °C for 80 s, with coverage of 6.5% (b). The solid line represents the result of a fit of the normalized dot radius distribution using the function $F(y)=[\beta_r^{\beta_r}/\Gamma(\beta_r)]y^{\beta_r-1}\exp(-\beta_r y)$, with $\beta_r=8$.

tributed to the following reason: when two capture zones overlap the respective dots impinge each other, and the radius of the final dot is taken as the sum of the two dots radii. This produces a fictitious increase of the size dispersion, i.e., an increase of the $f(r_d)$ FWHM curves. This is typical of random nucleation process where the exclusion zone does not play a role.¹⁷ The impingement event increases with the coverage. The probability to have a dot pairs at substrate coverage of about 15%, or 3 impinged dots at coverage of about 30%, is about 10%. So the relatively high probability to have impingement events gives rise to the observed low values of β_r .

There is another aspect of relevance, which should be discussed. The values of β_r found in the range of coverage where the coalescence probability is negligible, are high also at coverage lower than 5%. In this range however no correlation of the dot size with the capture radius has been found, as demonstrated by the results of Fig. 7. This apparent discrepancy can be explained with the possible contribution of the monomer evaporation during the deposition, which in the calculation of the capture sizes has not been taken into account. It should be considered, in fact, that for very low coverage the dots are quite distant from each other. Since the mean free path of the diffusing monomers is extremely short compared to the interisland separation, at low coverage the monomer can evaporate, rather than contributing to the dot growth.³⁰ In such a situation, all the monomers falling within the effective capture zone, will contribute to the dot growth process, thus giving rise to the scaling characteristic of the $f(r'_d)$, and to the high value of β_r . The monomers which fall outside of the effective capture region can either contribute to a new nucleation event or evaporate. So at very low coverage the real capture size could be smaller than what we have calculated. This leads, in this range of very low coverage to a poor correlation between the calculated capture size

TABLE I. Comparison between the values of β_r obtained from the fit of the frequency distribution $f(r'_d)$ relative to the scaled dot radius, through the equation $F(y)=[\beta_r^{\beta_r}/\Gamma(\beta_r)]y^{\beta_r-1}\exp(-\beta_r y)$, and the polydispersity ratio $\langle r_d \rangle^2/std_r^2$ between the first two moments of the frequency distribution $f(r_d)$ relative to the dot radius.

Coverage θ	β_r	$\langle r_d \rangle^2/std_r^2$
0.018	7	8
0.027	7	7
0.065	8	8.2
0.083	7	6.7
0.140	6	6
0.141	8	7.3
0.145	8	7.8
0.150	5	3.7
0.280	4	3

and the dot size, hence to the low values of σ (see Fig. 7). On the other hand, this mechanism gives rise to a dot size distribution typical of self-similar systems, hence to the good correlation between the data points and the fit (see values of Table I), because the monomer diffusion within the effective capture region is still taking place. In the range of coverage where the evaporation is negligible, we can estimate the Si adatoms diffusivity on the SiO₂ substrate. By approximating the length the adatoms must make before aggregating onto the dot to about one-half the minimum edge distance, $\langle d \rangle/2$, and by taking into account the lowest deposition time where appreciable nucleation is found, we estimate through the Einstein relation, a lower limit for the adatom diffusivity of about 2×10^{-16} cm²/s.

IV. CONCLUSIONS

In conclusion, a suppression of the nucleation of Si nanodots is observed in the neighborhood of pre-existing dots during RTCVD. This is attributed to the silicon adatoms capture mechanism during the deposition. The calculation of the capture zone in case of continuous nucleation is performed. A correlation between the final dot size and the available capture zone is found and this effect is shown to increase with increasing the substrate coverage. No role of the capture zone is observed at very low coverage due to the adatoms evaporation contribution. The data on the dot size distribution are fitted by using a scaling model based on the modification of the Voronoi tessellation. From the fit to the data a very high percentage (30%) of nucleation sites of the substrate is found to be deactivated by the nearest neighbor exclusion mechanism.

ACKNOWLEDGMENTS

The activity is funded by the IST project ADAMANT (No. IST-2001-34234). We gratefully acknowledge C. Bongiorno for his expert technical assistance during TEM imaging.

- *Electronic address: rosaria.puglisi@imm.cnr.it
- ¹S. Yamazaki, *Jpn. J. Appl. Phys.* **10**, 1023 (1971).
 - ²S. Tiwari, F. Rana, K. Chan, H. Hanafi, W. Chan, and D. Buchanan, *Proceedings of IEEE International Electron Devices Meeting*, 1995, p. 521.
 - ³K. Yano, T. Ishii, T. Sano, T. Mine, F. Murai, T. Hashimoto, T. Kobayashi, T. Kure, and K. Seki, *Proc. IEEE* **87**, 633 (1999).
 - ⁴B. D. Salvo *et al.*, *Proceedings of International electron devices meeting*, 2003, p. 597.
 - ⁵S. Lombardo, C. Gerardi, D. Corso, G. Ammendola, I. Crupi, and M. Melanotte, *Proceedings of non volatile semiconductor memory workshop*, 2003, p. 69.
 - ⁶J. D. Blauwe *et al.*, *Proceedings of International Electron Devices Meeting, Technical Digest* (IEEE, Piscataway, NJ, 2000), p. 683.
 - ⁷J. Vizoso, F. Martin, X. Martinez, M. Garriga, and X. Aymerich, *Microelectron. Eng.* **48**, 431 (1999).
 - ⁸S. Miyazaki, Y. Hamamoto, E. Yoshida, M. Ikeda, and M. Hirose, *Thin Solid Films* **369**, 55 (2000).
 - ⁹F. Mazen, T. Baron, G. Bremond, N. Rochat, P. Mur, and M. Semeria, *J. Electrochem. Soc.* **150**, G203 (2003).
 - ¹⁰C. M. Compagnoni, D. Ielmini, A. S. Spinelli, A. L. Lacaita, C. Previtali, and C. Gerardi, *Reliability Physics Symposium Proceedings*, 2003, p. 506.
 - ¹¹G. Nicotra, R. A. Puglisi, S. Lombardo, C. Spinella, M. Vulpio, G. Ammendola, M. Bileci, and C. Gerardi, *J. Appl. Phys.* **95**, 2049 (2004).
 - ¹²R. A. Puglisi, G. Nicotra, S. Lombardo, C. Spinella, G. Ammendola, M. Bileci, and C. Gerardi, *Surf. Sci.* **550**, 119 (2004).
 - ¹³R. A. Puglisi, G. Nicotra, S. Lombardo, C. Spinella, and C. Gerardi, *Mater. Res. Soc. Symp. Proc.* **788**, L12.2.1 (2004).
 - ¹⁴T. D. Lowes, *J. Appl. Phys.* **73**, 4937 (1993).
 - ¹⁵G. R. Carlow, R. J. Barel, and M. Zinke-Allmann, *Phys. Rev. B* **56**, 12 519 (1997).
 - ¹⁶M. Krishnamurty, J. Druker, and J. Venables, *J. Appl. Phys.* **69**, 6461 (1991).
 - ¹⁷M. Brinkmann, F. Biscarini, C. Taliani, I. Aiello, and M. Ghedini, *Phys. Rev. B* **61**, R16 339 (2000).
 - ¹⁸L. Rontzsch, K. H. Heinig, and B. Schmidt, *Poster communication at 33rd European solid-state device research conference*, 2003.
 - ¹⁹G. Nicotra, S. Lombardo, R. Puglisi, C. Spinella, G. Ammendola, and C. Gerardi, *Proc. Inst. Phys. Conf. Ser.* **180**, 119 (2003).
 - ²⁰G. Nicotra, S. Lombardo, C. Spinella, G. Ammendola, C. Gerardi, and C. Demuro, *Appl. Surf. Sci.* **205**, 304 (2003).
 - ²¹R. Okada and S. Iijima, *Appl. Phys. Lett.* **58**, 1662 (1991).
 - ²²C. Single, F. Zhou, H. Heidemeyer, F. E. Prins, and E. Plies, *J. Vac. Sci. Technol. B* **16**, 3938 (1998).
 - ²³J. Omachi, R. Nakamura, K. Nishiguchi, and S. Oda, *Mater. Res. Soc. Symp. Proc.* **638**, F5.3.1 (2001).
 - ²⁴A. Nakajima, Y. Sugita, K. Kawamura, H. Tomita, and N. Yokoyama, *Jpn. J. Appl. Phys., Part 2* **35**, L189 (1996).
 - ²⁵C. Spinella, S. Lombardo, and F. Priolo, *J. Appl. Phys.* **84**, 5383 (1998).
 - ²⁶C. Ratsch and J. A. Venables, *J. Vac. Sci. Technol. A* **215**, S96 (2003).
 - ²⁷I. Markov, *Thin Solid Films* **8**, 281 (1971).
 - ²⁸P. A. Mulheran and J. A. Blackman, *Philos. Mag. Lett.* **721**, 55 (1995).
 - ²⁹P. A. Mulheran and J. A. Blackman, *Phys. Rev. B* **53**, 10 261 (1996).
 - ³⁰D. A. Robbie and P. A. Mulheran, *Philos. Mag. B* **80**, 1299 (2000).